*Avestia Publishing*
*Journal Name: Journal of Fluid Flow, Heat and Mass Transfer (JFFHMT)*
*Volume 13, Year 2026*
*ISSN: 2368-6111*
*DOI: 10.11159/jffhmt.2026.001*

# Numerical Investigation of Porosity Effects on the Thermo-Hydraulic Performance of a Kagome-Lattice Duct in a Conjugate Problem

**Giacomo Tosatti[1], Sandra Corasaniti[1], Michele Potenza[1], Ivano Petracci[1,*]**
[1] Department of Industrial Engineering, University of Rome "Tor Vergata"
via del Politecnico n.1, 00133 Rome, Italy
giacomo.tosatti@students.uniroma2.eu; sandra.corasaniti@uniroma2.it, michele.potenza@uniroma2.it, ivano.petracci@uniroma2.it (*corresponding author)

***Abstract*** *- The compactness of electronic devices and mechanical components and the constant increase in power density pose significant challenges in thermal management. These geometric constraints imply a reduced length of the channels dedicated to cooling, hence the need to properly analyse the conjugate heat transfer problem and develop innovative heat dissipation systems, such as lattice structures. This paper aims to numerically investigate the thermo-fluid dynamics properties of a short, empty duct, hence with porosity $\phi$ = 100%, named K0, 80 mm long, with a cross-section of 15 x 5 mm, in two different flow conditions: fully developed and developing flow. Then, the same channel is equipped with a Kagome-truss lattice with a truss diameter of 0.8 mm, designated as K1, characterised by a porosity of $\phi$ = 87%, and the analysis is repeated for both outflow conditions. The fluid is air, and the operating Reynolds numbers range from 2852 to 17115, thus falling within the transitional flow regime. Results for the smooth duct demonstrate its sensitivity to flow conditions, revealing a substantial increase in the Nusselt number by up to 13% at the cost of a higher friction factor, as expected from existing studies available in the literature. On the contrary, no significant variation in both the friction factor and the Nusselt number is observed for the K1, suggesting that its thermo-fluid dynamic properties are more influenced by the lattice structure rather than the flow profile. Finally, the two ducts are compared in terms of energy efficiency, evaluated as $Nu/\lambda^{1/3}$, revealing that at the same Reynolds number, the efficiency of the Kagome duct is up to 2.2 and 2.4 times greater than that of the empty duct in fully developed and developing flow conditions, respectively. After the independence of the entry length for the K1 duct had been verified, the analysis was extended to two additional porosities, namely 96% and 76%, to assess whether an optimum in heat exchange and energy efficiency could be found. Results showed that increasing the pillar diameter leads to higher heat while leaving the flow pattern unchanged; however, the rise in pressure drop causes a saturation of the energy efficiency.*

***Keywords***: RANS Numerical Simulations; Conjugate Entry Length Problem; Kagome Lattice Channel; Smooth Duct; Porous Media; Convective Heat Transfer; Pressure Losses



## 1. Introduction

In industrial design, some of the most critical challenges include geometric and spatial constraints, such as those encountered in compact heat exchangers. These constraints result in a limited length of the cooling channels, hence the comprehension of the conjugate problem, which involves the simultaneous development of both the hydrodynamic and thermal boundary layers, becomes critical. Furthermore, since the flow is not fully developed, the range of Reynolds numbers that determine its regime is significantly affected and often falls within the transitional regime, a condition which has been experimentally studied by a wide range of researchers, such as Gnielinski [1], Churchill [2] and Tam and Ghajar [3].

*Date Received: 2025-04-10*
*Date Revised: 2025-10-09*
*Date Accepted: 2025-11-11*
*Date Published: 2026-01-12*

These limitations, combined with the need to dissipate an ever-growing thermal power to ensure the correct functionality and preservation of mechanical and electronic components, have driven scientific research toward the development of innovative heat dissipation systems. Porous and periodic cellular materials (PCM) are highly promising multifunctional materials, with broad applications ranging from the aerospace and automotive sectors [4] to energy storage and heat transfer systems [5]. Among PCMs, truss-based PCMs carved out a prominent spot due to their superior structural resistance to both static and dynamic loads [6] and their heat dissipation capability, which can reach values up to seven times higher than that of an empty channel with a lower pressure drop compared to other non-truss-based options, leading to a thermal efficiency that outperforms typical heat sink media such as pin fins and cylinder banks [7]. Among truss-based lattices, the Kagome type exhibits isotropic mechanical responses under compression and shear and, unlike tetragonal PCMs, this behaviour remains unchanged after yielding [8]. Moreover, Kagome lattices provide a higher heat dissipation rate, up to 38%, for a fixed pumping power compared to the tetragonal counterpart, reaching values comparable to the X-type lattice [9]. For these reasons, several additional studies have been conducted to optimise Kagome performances further. Joo et al. [10] investigated the heat transfer capabilities of wire-woven bulk Kagome (WBK) made of aluminium helix wires in forced convection, analysing the effect of Kagome orientation as well by altering the flow pattern. The results showed that the "most closed" orientation possesses a considerably higher Nusselt number for each tested flow rate at the cost of a slightly increased pressure drop. However, the findings from Shen et al. [11] showed that the truss-cored Kagome achieves an overall Nusselt number up to 26% higher than a WBK, while maintaining a similar pressure drop. This is because a large portion of the ligaments is near the walls of the employed sandwich panels and so the flow blockage increases, leading to the formation of low-momentum vortices.

Although several studies have investigated heat transfer enhancement in lattice or porous structures, most available results in the literature concern sandwich panels, which can be regarded as ducts whose cross section is characterized by one side length largely exceeding the other one. In such configurations, the interaction between the channel's perpendicular walls is negligible. Conversely, in the present study, the cross-sectional dimensions are comparable, resulting in mutual interactions between orthogonal walls that significantly influence the fluid pattern. Furthermore, previous works have mainly focused on fully developed flow, neglecting the effects of inlet length and conjugate heat transfer. The present work addresses these gaps by performing a systematic numerical and experimental analysis of compact lattice heat dissipation media, evaluating the combined effects of porosity, flow regime, and inlet length on both local and global thermohydraulic performance, expanding on the results found by this same research group in previous published studies on an X-type lattice [12–14].

The pressure drop, heat dissipation capability and thus thermal efficiency of a short smooth duct, namely K0, in which the working fluid is air, are investigated under two different flow conditions: fully developed flow and a flat inlet velocity profile, thereby accounting for inlet and outlet effects. Subsequently, the same analysis will be repeated on a duct equipped with the Kagome lattice, labelled K1, featuring a cell staggering equal to half the characteristic cell size in the transition from the first to the second row, which is then repeated periodically along the whole duct. The total porosity $\phi$ of the channel, defined as the ratio of the void to the entire internal volume, is set to be 87%. Obviously, for the K0 duct, the porosity is 100%. Results show that heat transfer is independent of the thermofluid entry length, thus demonstrating the advantage of using these heat dissipation media as highly compact solutions.

Afterwards, a topological analysis is conducted on the pillar size by decreasing and increasing their diameter, yielding porosities of 96% and 76% for the thinnest and thickest pillars, respectively. This analysis showed that, as porosity decreases from the highest to the lowest, the heat transfer rate doubles. This enhancement is to be attributed to the increased heat exchange area, rather than any modification of the flow pattern. This improvement, however, is accompanied by a rise in pressure losses and thus a saturation of the energy efficiency is found, indicating that there is a limit to how thick these pillars can be.

## 2. Numerical methodology

### 2.1. Governing equations

The governing equations of the problem under investigation are the three Navier-Stokes equations, namely the conservation of mass, momentum and energy. Assuming the fluid to be incompressible, they can be written as shown in Eqs. (1) – (3):

$$\frac{\partial u_i}{\partial x_i} = 0 \tag{1}$$

$$\frac{\partial u_i}{\partial t} + u_j \frac{\partial u_j}{\partial x_j} = -\frac{1}{\rho}\frac{\partial \mathrm{p}}{\partial x_i} + \nu \frac{\partial^2 u_i}{\partial x_j \partial x_j} \tag{2}$$

$$\frac{\partial T}{\partial t} + u_j \frac{\partial T}{\partial x_j} = \alpha \frac{\partial T^2}{\partial x_j \partial x_j} \tag{3}$$

Indeed, a direct approach to directly solve these equations would be impractical, hence the choice to adopt a RANS approach, decomposing the flow variables of the three equations as shown in Eq. (4) for velocity:

$$u_i = \bar{u}_i + u_i' \tag{4}$$

where $\overline{u}_i$ is the time-averaged quantity and $u_i'$ the fluctuating term. By substituting the decomposed variables back into the instantaneous form of the Navier-Stokes equations, the time-averaged equations are obtained as follows in Eqs. (5)–(7).

$$\frac{\partial U_i}{\partial x_i} = 0 \tag{5}$$

$$\frac{\partial U_i}{\partial t} + U_j \frac{\partial U_i}{\partial x_j} = -\frac{1}{\rho}\frac{\partial P}{\partial x_i} + \frac{\partial}{\partial x_j}\left(\nu \frac{\partial U_i}{\partial x_j} - \overline{u_i' u_j'}\right) \tag{6}$$

$$\frac{\partial T}{\partial t} + U_j \frac{\partial T}{\partial x_j} = \frac{\partial}{\partial x_j}\left[k \frac{\partial T}{\partial x_j} - \overline{T' u_j'} + \frac{\mu}{\rho c}\left(\frac{\partial U_i}{\partial x_j}\right)\right] \tag{7}$$

The overbarred terms $\overline{u_i' u_j'}$ and $\overline{T' u_j'}$ are the Reynolds stresses tensor and turbulent heat flux respectively. These terms describe the influence of the instantaneous components on the mean flow field and, according to the Boussinesq' hypothesis, they are modelled as:

$$-\overline{u_i' u_j'} = \nu_t \left(\frac{\partial u_i}{\partial x_j} + \frac{\partial u_j}{\partial x_i}\right) - \frac{2}{3}\left(k + \nu_t \frac{\partial u_i}{\partial i}\right)\delta_{xj} \tag{5}$$

$$k = \frac{1}{2}\left(\overline{u_1'^2} + \overline{u_2'^2} + \overline{u_3'^2}\right) \tag{6}$$

$$-\overline{T' u_j'} = k_t \frac{\partial T}{\partial x_j} \tag{7}$$

where $\nu_t$ is the eddy kinematic viscosity, $k_t$ the turbulent thermal conductivity, $k$ the turbulent kinetic energy. The problem is then reduced to the sole determination of the unknown variable $\nu_t$, which is modelled with two auxiliary equations in the so-called two equations turbulence models. In the present work the *k-ω SST* by Menter [15] is employed, combining the *k-ω* formulation in the innermost part of the boundary layer (i.e., near the walls) to accurately resolve the strong gradients, and the robustness of the k-ε model in the free stream. The equations for $k$ and $\omega$ are as follows:

$$\frac{\partial k}{\partial t} + u_j \frac{\partial k}{\partial x_j} = \frac{\partial}{\partial x_j}\left[\left(\nu + \sigma^* \frac{k}{\omega}\right)\frac{\partial k}{\partial x_j}\right] + \overline{u_i' u_j'}\frac{\partial u_i}{\partial x_j} - \beta^* k\omega \tag{8}$$

$$\frac{\partial \omega}{\partial t} + u_j \frac{\partial \omega}{\partial x_j} = \frac{\partial}{\partial x_j}\left[\left(\nu + \sigma \frac{k}{\omega}\right)\frac{\partial \omega}{\partial x_j}\right] + \frac{\alpha\omega}{k}\overline{u_i' u_j'}\frac{\partial u_i}{\partial x_j} - \beta k\omega + \frac{\sigma_d}{\omega}\frac{\partial \omega}{\partial x_j}\frac{\partial k}{\partial x_j} \tag{9}$$

More details on the variables and constants of the equations above can be found in [16]. It should be noted that in the present work, all time derivatives are identically zero, as the problem is studied under steady state conditions.

### 2.2. Grid generation

As mentioned in both the abstract and the introduction section, two different types of ducts are considered. The first one is a smooth aluminium channel, 80 mm long, with a flow cross-section of 15 mm by 5 mm, while the mantle's thickness is set to 0.7 mm. An additional 35 mm long duct is added after the heated channel to avoid any type of outlet influence on the velocity gradients and thus on the heat transfer mechanism.

A structured mesh is employed, given the simplicity of the studied geometry; both fluid and solid are discretised with a single block each. The 15 mm side needed 90 nodes while the shorter side only 40 to guarantee a $y^+$ <1 and a growth ratio equal to 1.15 utilizing a bigeometric growth law. Then, one element per millimetre of the channel's length is employed to discretize the streamwise direction.

The boundary conditions are illustrated in Fig. 1 and summarised briefly in Table 1. A velocity inlet boundary condition, coloured in red, is applied at the start of the domain. At the same time, a pressure outlet with a gauge pressure of 0 Pa is imposed on the far end, as indicated by the cyan surface. Six different volumetric flow rates are tested, ranging from 25 l/min to 150 l/min in increments of 25 l/min. A uniform heat flux $q''$ equal to 13700 W/m² is applied on the channel's outer mantle, coloured in light green. The internal walls of the channel are treated as no-slip walls: the blue wall is considered to be diabatic, while the orange one is adiabatic. Given

the symmetry of the domain, only half of it is modelled; however, the symmetry plane is not reported in Fig.1 for clarity purposes.

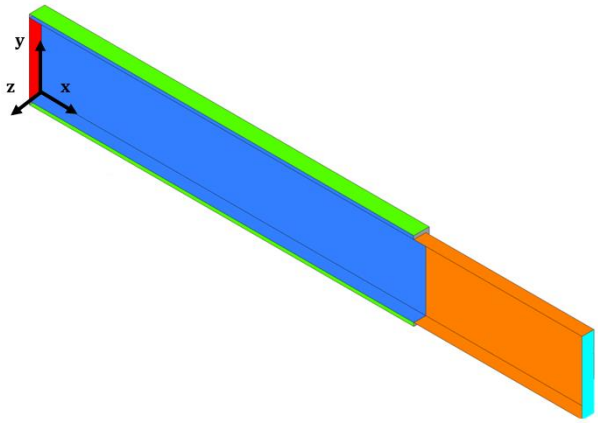


Fig. 1: Isometric view of the smooth domain.

Tab. 1: Volumetric flow rates, corresponding velocities and Reynolds number

| **Boundary Condition** | **Colour** |
|---|---|
| Velocity inlet | Red |
| No slip diabatic wall | Blue |
| No slip adiabatic wall | Orange |
| Heated wall | Green |
| Pressure outlet | Cyan |
| Symmetry | Not shown |

As far as the inlet condition is concerned, in the fully developed flow case, an additional simulation in a very long duct (20 times the length reported above) for each flow rate was performed to ensure an appropriate entry length for the fluid, thus obtaining a fully developed profile for the velocity field and the turbulent transport quantities (i.e. $k$ and $\omega$), which are then used as entry conditions. In contrast, velocities are constant in the developing flow case, hence a flat velocity profile is applied. The turbulent kinetic energy and dissipation rate are carefully set to match the average values of their counterparts in the first case.

A representation of the Kagome lattice can be found in Fig. 2. The base cell is modelled in its entirety in the first row, with offset equal to half its characteristic length in the second row. The lattice then repeats itself periodically for the 80 mm length of the channel.

An additional section, 35 mm long, was added after the inlet section, contrary to the smooth case, to avoid convergence issues during the simulation. A fully unstructured poly-hexahedral mesh was employed to reduce the total element count and minimise numerical diffusion compared to tetrahedral elements. The first cell height is set to obtain a $y^+<1$ and 13 layers are grown from each wall with a last-ratio approach to guarantee a growth ratio equal to 1.15 and a smooth transition to the hexa volume mesh. The boundary conditions remained unchanged, the lattice was treated as a no-slip diabatic wall.

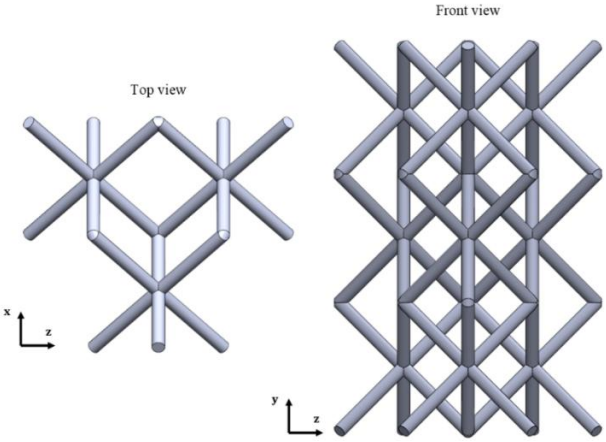


Fig. 2: Top and front view of the first two rows of the Kagome lattice.

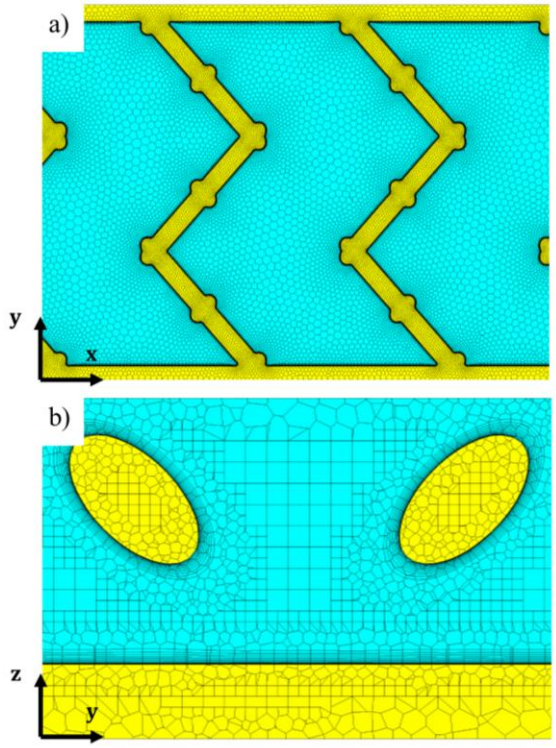


Fig. 3: Employed poly-hexa mesh. a) Surface mesh on the symmetry plane. b) Volume mesh.

A close-up of the surface mesh on the symmetry plane can be found in Fig.3a, while a detail of the volume mesh can be appreciated in Fig.3b.

All the simulations are carried out with the Ansys FLUENT software. The equations for momentum, energy, pressure, TKE, and specific dissipation were discretised using a second-order upwind scheme, and the simulations were considered converged when the residuals of continuity, momentum, energy, TKE and specific dissipation reached a value of $10^{-10}$ for the smooth pipe, which was achieved under 500 iterations, and $10^{-6}$ for the Kagome case.

## 3. Results

### 3.1. Mesh validation

Six different flow rates have been simulated, and the results were compared in terms of the friction factor λ and the Nusselt number Nu, whose equations are reported in Eqs (10)-(11), respectively, with the famous works available in open literature. In particular, a convergence and mesh independence study was conducted for the fully developed flow case, comparing the results to the Blasius and Dittus-Boelter correlations, which are presented in Eqs. (12)-(13).

$$\lambda_{hydr} = \frac{2\Delta P D_{hydr}}{\rho L u^2} \tag{10}$$

$$Nu_{hydr} = \frac{hD_{hydr}}{k}; h = \frac{q''}{(T_{wall} - T_{bulk})} \tag{11}$$

$$\lambda_{Blasius} = \frac{0.316}{Re_{hydr}^{0.25}} \tag{12}$$

$$Nu_{Dittus-Boelter} = 0.023 Re_{D_{hydr}}^{0.8} Pr^{0.3} \tag{13}$$

The thermophysical properties of the air were considered constant and evaluated at an inlet temperature of 20°C. The mass-average of the pressure drop and bulk temperature were considered when estimating the convective heat transfer coefficient $h$ in Eqs. (10)-(11) respectively.

Table 2 provides an overview of the carried-out simulations, while Fig. 4 shows the comparison of the friction factor and Nusselt number to Blasius' and Dittus-Boelter's correlations. The results are deemed satisfactory; therefore, the previously described mesh was chosen to extend the investigation to the developing flow profile.

Tab. 2: Volumetric flow rates, corresponding velocities and Reynolds number.

| $\dot{V}\left[\frac{l}{min}\right]$ | $u\left[\frac{m}{s}\right]$ | $Re_{D_{hydr}}$ |
|---|---|---|
| 25 | 5.55 | 2852 |
| 50 | 11.11 | 5704 |
| 75 | 16.66 | 8557 |
| 100 | 22.22 | 11410 |
| 125 | 27.77 | 14262 |
| 150 | 33.33 | 17115 |

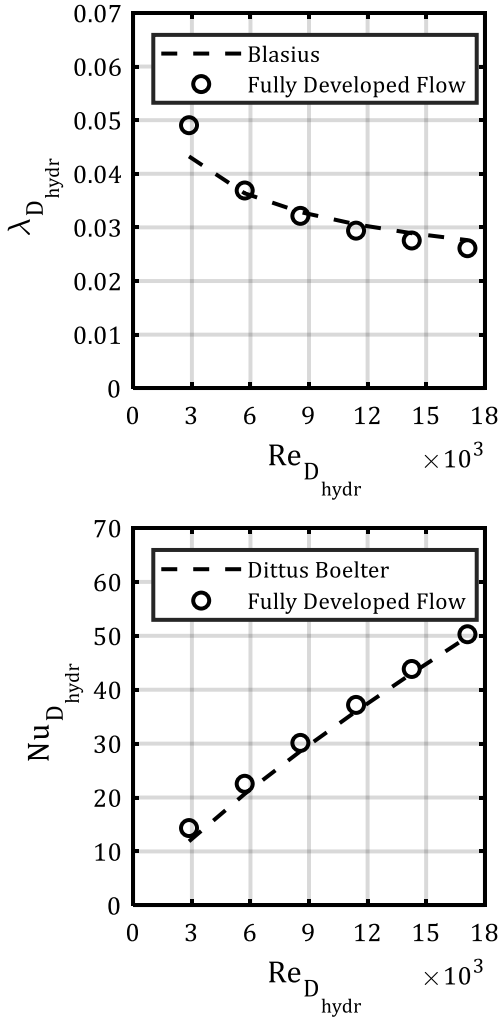


Fig. 4: Comparison between numerical results for the K0 duct ($\phi$ = 100%) in fully developed flow conditions and correlations available in the literature.

Three different meshes were studied for the Kagome duct, generated by varying the number of hexahedral elements while keeping the number of inflation layers unchanged. The total element count amounts to 5.5, 7.8, and 11 million fluid elements for the coarse, medium, and fine grids, respectively. Table 3 presents the analysis results in terms of friction factor and Nusselt number for the three tested grids, obtained at a volumetric flow rate of 150 l/min. Since the percentage difference between the medium and fine meshes is 0.47% for λ and 0.33% for Nu, the medium grid has been used for the simulations.

Tab. 3: Mesh independence study; parameters and output.

| N° elements | $\lambda_{D_{hydr}}$ | $Nu_{D_{hydr}}$ | $\Delta\lambda_{D_{hydr}}$ [%] | $\Delta Nu_{D_{hydr}}$ [%] |
|---|---|---|---|---|
| $5.5 \cdot 10^6$ | 1.592 | 264.40 | / | / |
| $7.8 \cdot 10^6$ | 1.637 | 277.38 | 2.73% | 4.90% |
| $11 \cdot 10^6$ | 1.629 | 278.29 | 0.47% | 0.33% |

### 3.2. Entry length influence

A thorough comparison of all the proposed and tested cases is presented in the following figures.

Figure 5 shows the trends in friction factor and Nusselt number for the K0 pipe under both flow conditions. As expected, the flat velocity profile leads to an increase in the friction factor due to the higher wall shear. However, the resulting temperature profile exhibits a gradient that enhances heat transfer, leading to a higher Nusselt number. This result is compared with the Gnielinski correlation [1], highlighting the reliability of the obtained data.

The same analysis is repeated for the K1 duct and reported in Fig. 6, in which is possible to observe the independence of heat transfer from the flow condition, although a slight influence on the friction factor can still be noted. This suggests that it is the shape and arrangement of the lattice that determine its heat transfer characteristics, not the entry length.

Finally, Fig. 6 also highlights the thermal efficiency $\varepsilon$ of the two pipes, obtained from dimensional analysis as in Eq. (14):

$$Q \sim \Delta P u L^3 \qquad \lambda \sim \frac{\Delta P}{u^2} \qquad Re \sim uL$$
$$Q \sim \lambda Re^3 \qquad \varepsilon = \frac{Nu}{\lambda^{\frac{1}{3}}} \tag{14}$$

where $Q$ is the pumping power.

From this figure, the advantage of the K1 channel over its smooth counterpart is clearly evident, as efficiencies up to 2.2 times higher can be achieved in the case of fully developed flow, and 2.4 times greater for the developing flow.

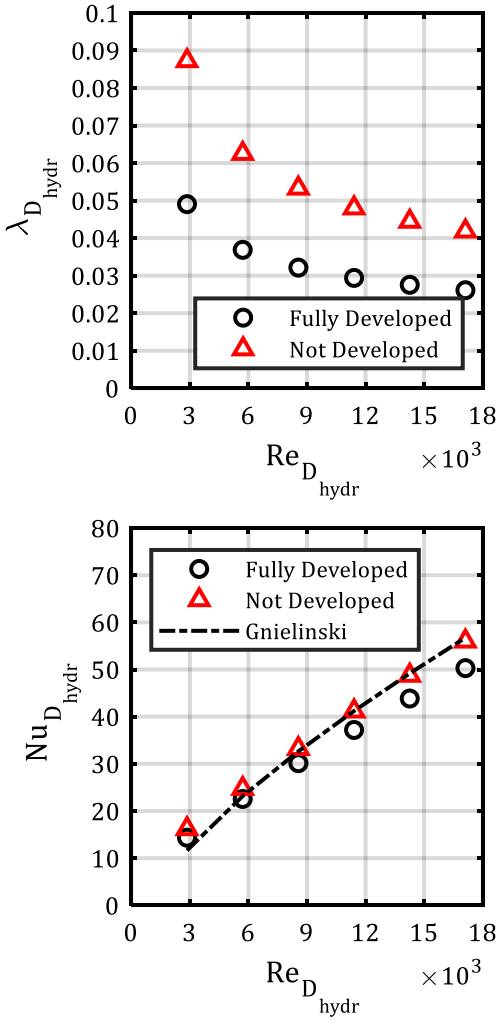


Fig. 5: Comparison between the fully developed and developing flow cases, K0 duct ($\phi$ = 100%).

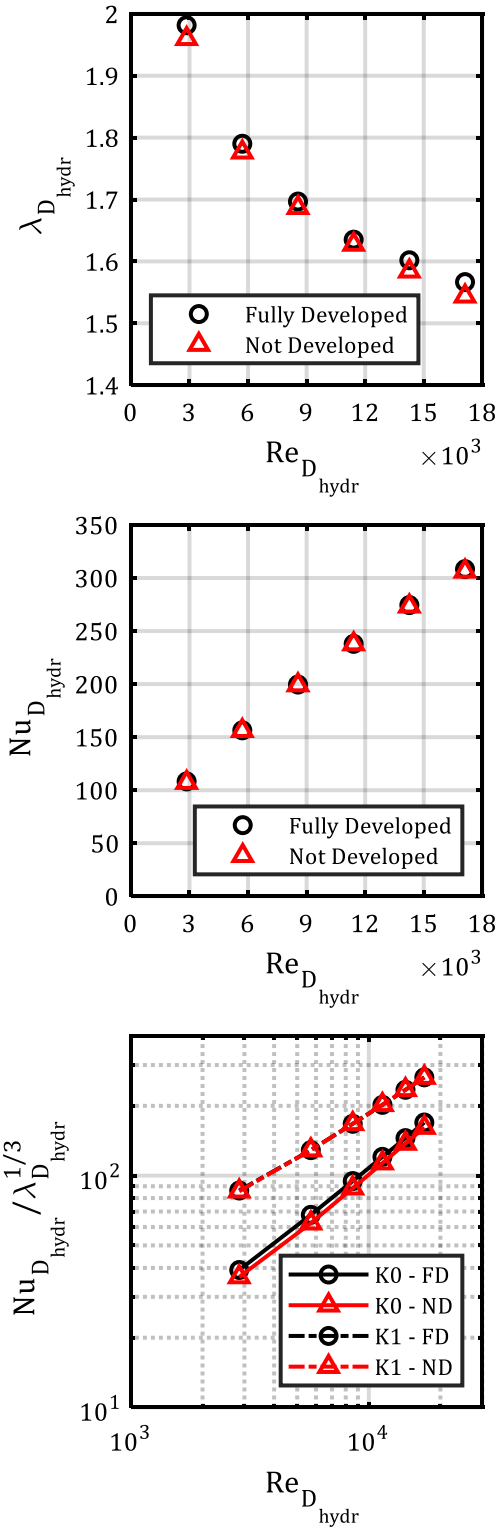


Fig. 6: Comparison between fully developed and developing flow cases in the K1 duct ($\phi$ = 87%). Thermal efficiency of the two channels as a function of Reynolds number.

### 3.3. Porosity effect

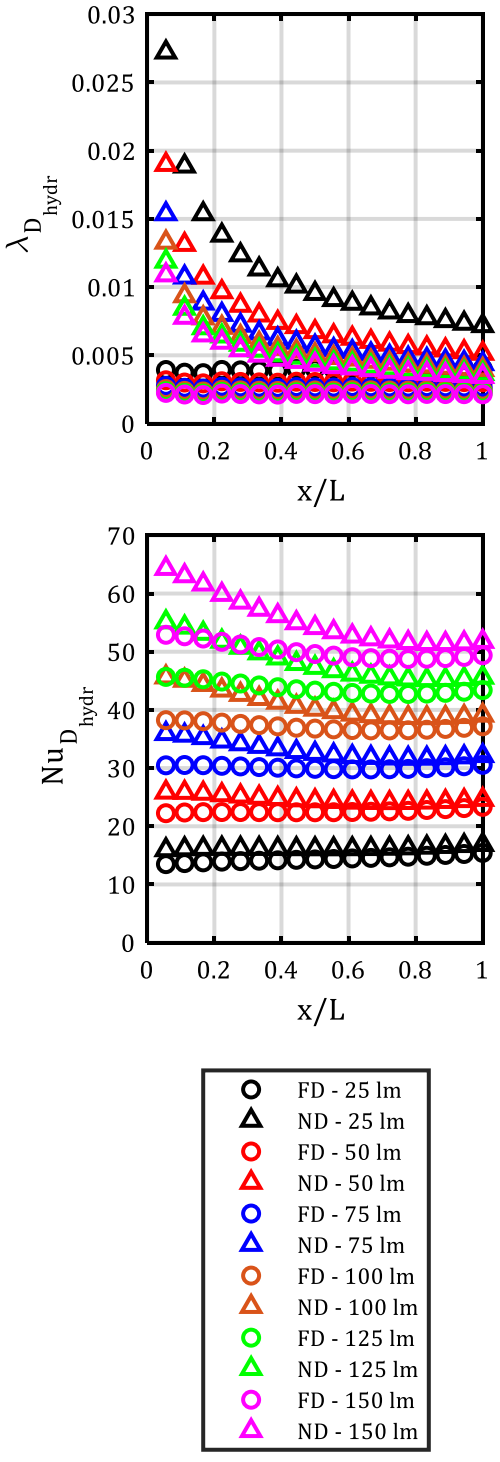


Fig. 7: Friction factor and Nusselt number for the 100% porosity case (K0 duct).

Once the independence from the entry length was established, the analysis focused on the effect of porosity. For the Kagome-lattice duct, in addition to the main configuration, denoted by a pillar diameter of 0.8 mm and a porosity of 87%, two further cases were investigated, with pillar diameters of 0.5 mm and 1.1 mm, achieving porosities of 96% and 76%, respectively.

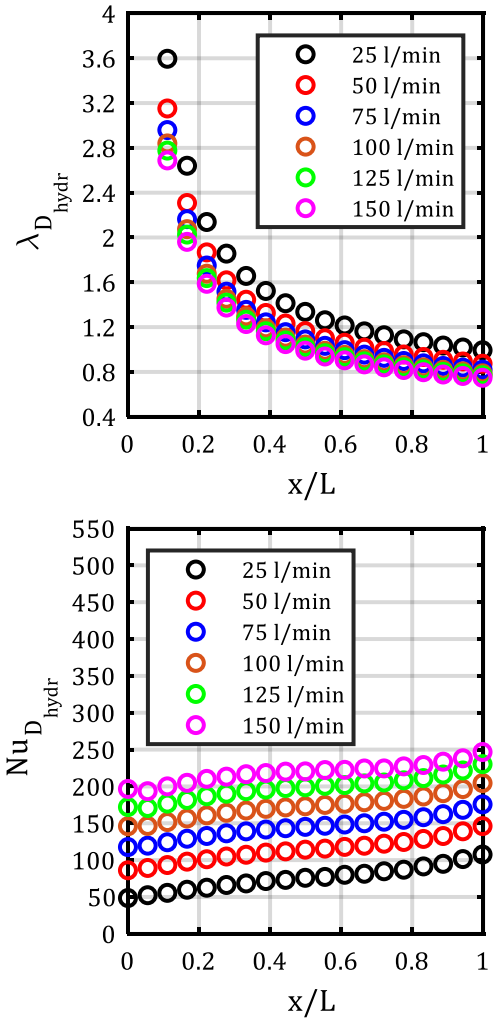


Fig. 8: Friction factor and Nusselt number for the 96% porosity case (K1 duct).

Figures 7, 8, 9 and 10 show the friction factor and the Nusselt number, calculated using Eqs. (15) and (16), as a function of the local coordinate for the four porosities in decreasing order. The equations are the following:

$$\lambda_{hydr}(x) = \frac{2 \cdot [p(x=0) - p(x)]}{\rho u^2} \cdot \frac{D_{hydr}}{x} \quad (15)$$

$$Nu_{hydr}(x) = \frac{h(x) D_{hydr}}{k} \quad (16)$$

$$h(x) = \frac{q''}{(T_{wall}(x) - T_{bulk}(x)}$$

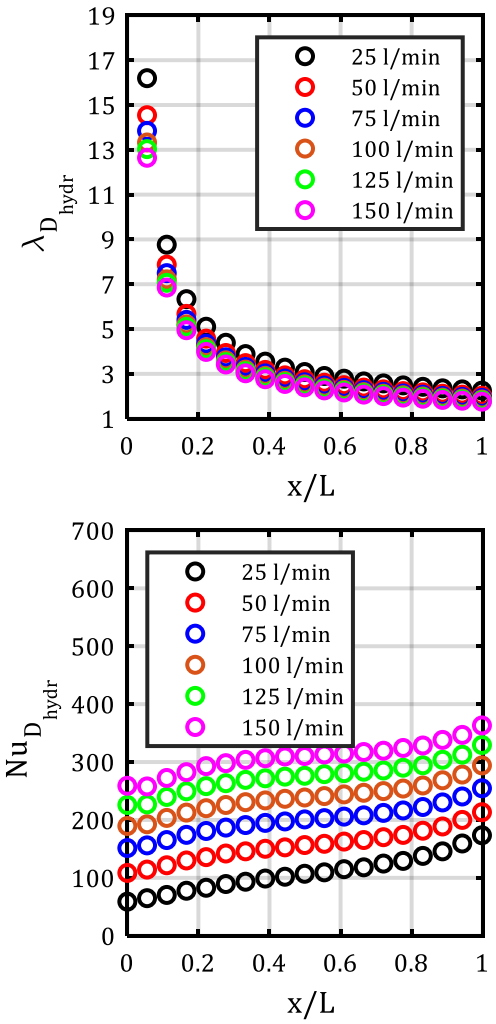


Fig. 9: Friction factor and Nusselt number for the 87% porosity case (K1 duct).

Considering the friction factor, the definition given in Eq. (15) implies that, for $x = L$, the pressure drop is evaluated over the entire duct length. Consequently, starting from the inlet section and progressing along the x-axis, the local friction coefficient approaches its average value. From these data, a peak is observed at the channel entrance, which then stabilizes around an asymptotic value starting approximately halfway along the duct length. Naturally, for the duct with maximum porosity (K0) under not fully developed flow conditions, as noted in the previous section, the coefficient is two orders of magnitude lower than for the Kagome ducts.

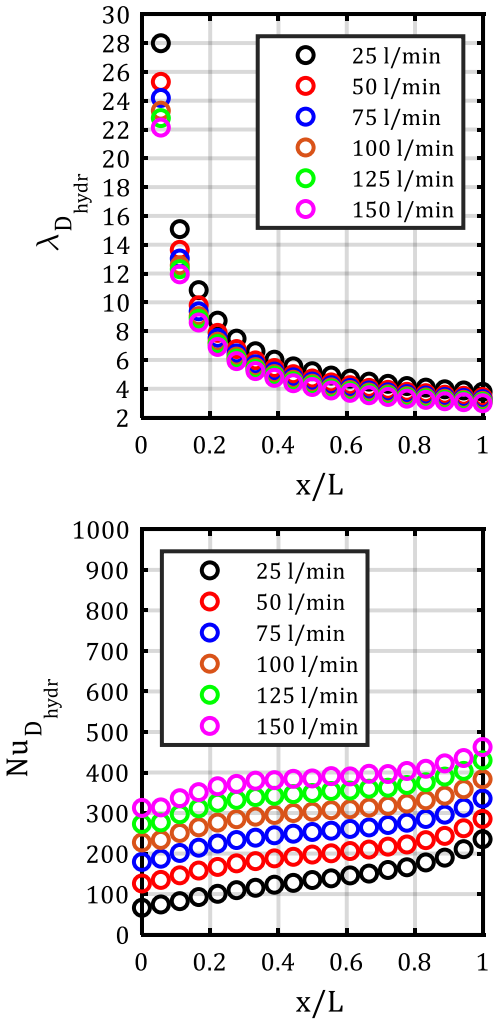


Fig. 10: Friction factor and Nusselt number for the 76% porosity case (K1 duct).

For heat transfer, however, the distinction between maximum porosity and all other cases is much more pronounced, particularly at higher flow rates. In the smooth K0 duct, the local Nusselt number, shown in Fig. 7, exhibits a peak at the duct entrance, where the heated section with constant heat flux begins, and then approaches an asymptotic value for larger axial positions, reaching a nearly constant value already at x/L=6. In contrast, as illustrated in Figs. 8-9-10, for the

Kagome duct, the inlet effect appears to have little influence on the local convective heat transfer coefficient, which increases slightly up to $x/L$=0.2, remains nearly constant until $x/L$=0.8, and then increases slightly near the outlet section. Overall, the Nusselt number shows a weaker dependence on inlet and outlet conditions, remaining almost uniform along most of the duct length. Therefore, the insensitivity to inlet length in K1 indicates that lattice-induced mixing dominates over boundary layer development.

Given that Kagome ducts are more effective in heat transfer than smooth ducts, the 100% porosity case will be excluded from subsequent comparisons with average values.

Figures 11 and 12 present the average friction coefficients and Nusselt numbers as functions of porosity and Reynolds number.

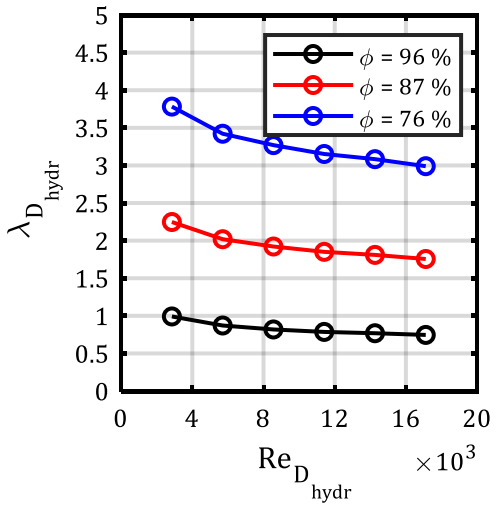


Fig. 11: Friction factor as a function of the Reynolds number; all tested porosities for K1 duct.

It is observed that a decrease in porosity (i.e., an increase in pillar diameter, resulting in a smaller cross-sectional flow area) tends to increase both of these thermo-fluid dynamic variables. As porosity decreases from a maximum of 96% to a minimum of 76%, heat transfer enhancements reach values close to 100% across all flow regimes.

It should be noted, however, that the friction factor increases by a factor of four when moving from the channel with the highest porosity to that with the lowest due to flow blockage; an aspect that must be considered in the design of such channels. Figures 13 and 14 highlight this characteristic.

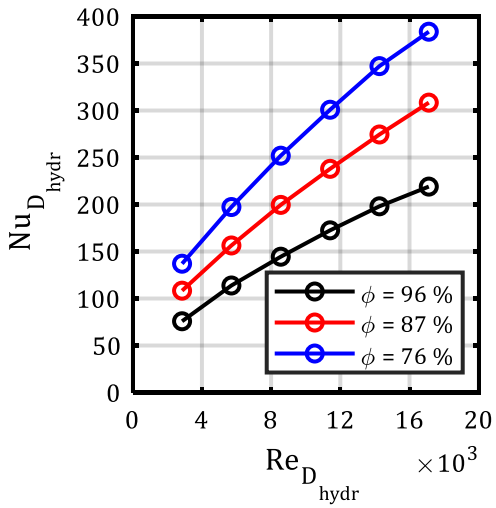


Fig. 12: Nusselt number as a function of the Reynolds number; all tested porosities for K1 duct.

In Fig. 13, it is evident that the medium-porosity duct outperforms the high-porosity one. However, this trend reaches a saturation as the porosity is further reduced.

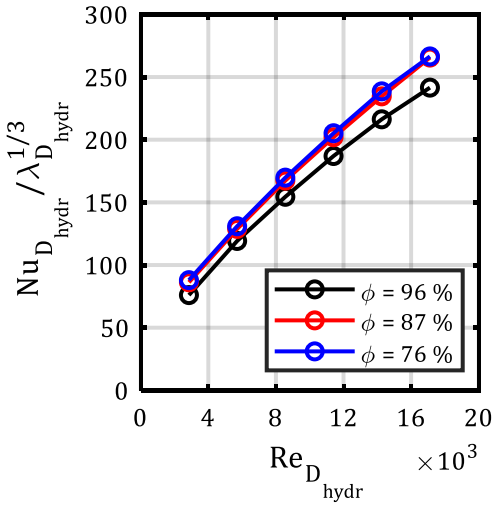


Fig. 13: Energy efficiency as a function of the Reynolds number; all tested porosities for K1 duct.

In Fig. 14, as porosity decreases, the data shift upward, indicating enhanced heat transfer for a fixed pumping power and thus for a fixed compressor dimension that feeds the circuit. Moreover, since the

slope of the trend remains nearly unchanged, it is possible to conclude that the fundamental heat transfer mechanism is preserved, and the increase in performance is mainly due to the larger surface area available for heat exchange rather than to changes in flow dynamics.

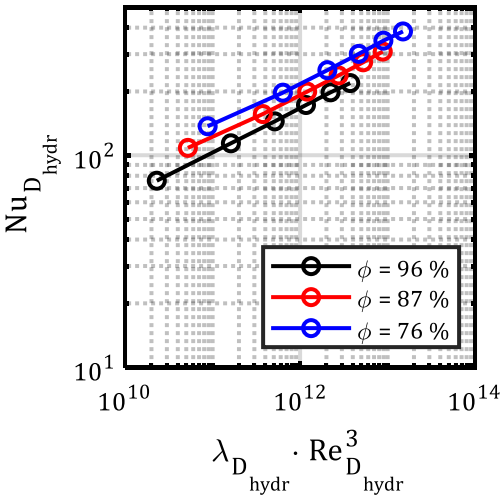


Fig. 14: Nusselt number as a function of pumping power for all tested porosities in the K1 duct.

This conclusion is confirmed by the velocity streamlines reported in Fig. 15. In this picture, obtained for an inlet flow rate of 100 l/min, it is shown that, regardless of the truss size, the helical flow pattern remains unchanged despite the varying local velocity peaks and, consequently, the degree of mixing remains constant.

## 5. Conclusion

A series of 3D RANS simulations was conducted on an empty rectangular-section channel, K0, for two different inflow conditions: fully developed and flat velocity profile. The same analysis was then repeated on the same channel equipped with a Kagome lattice, named K1. The results for the smooth channel demonstrated its sensitivity to the velocity profile, with a noticeable increase in the Nusselt number up to 13%.

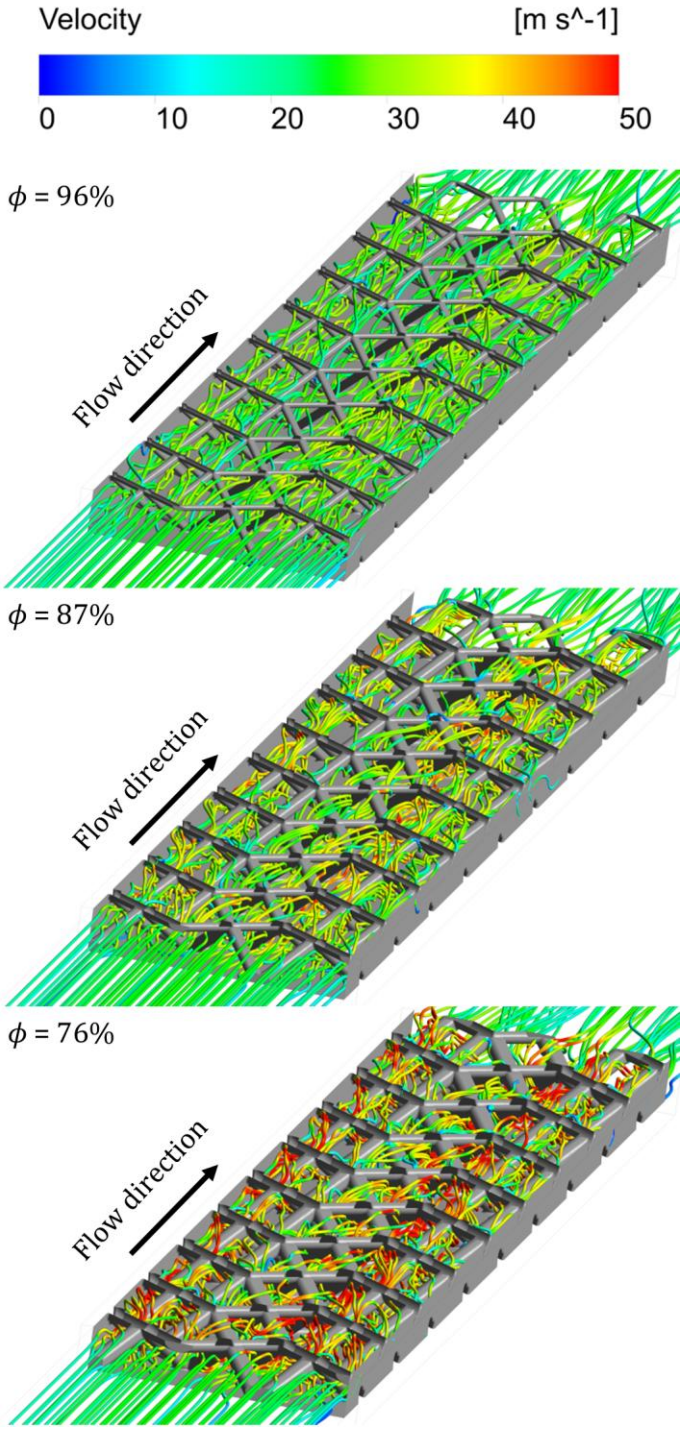


Fig. 15: velocity streamlines for each tested porosity of K1 duct. Inlet flow rate of 100 l/min.

However, this is followed by a greater pressure drop, leading to a lower thermal efficiency for every tested flow regime. The K1 duct showed no significant difference between the two inlet conditions, suggesting

that the lattice arrangement along the duct primarily influences its heat dissipation capabilities. Lastly, the K1 channel exhibited significantly higher thermal efficiency across all Reynolds numbers and flow conditions, reaching peak values up to 2.4 times those of the baseline case.

Once the entry length independence had been confirmed, a parametric analysis of the lattice channel revealed that decreasing porosity enhances both the friction factor and heat transfer, with the Nusselt number rising twofold between the two extremes of the investigated porosity range. This improvement comes at the cost of higher-pressure losses, which must be taken into account when selecting the compressor. The results also showed that the flow structure remains stable regardless of truss size, indicating that the enhanced heat transfer is primarily attributable to the increased heat exchange area. Finally, the energy efficiency trend suggests that there is no benefit in employing excessively dense structures, as this parameter reaches a saturation point.

## References


[1] Gnielinski, V., 1976, "New Equations for Heat and Mass Transfer in Turbulent Pipe and Channel Flow," International Chemical Engineering, **16**, pp. 359–368.

[2] Churchill, S. W., 1977, "Comprehensive Correlating Equations for Heat, Mass and Momentum Transfer in Fully Developed Flow in Tubes," Industrial & Engineering Chemistry Fundamamentals, **16**(1), pp. 109–116.

[3] Tam, L. M., 2006, "Transitional Heat Transfer in Plain Horizontal Tubes," *Heat Transfer Engineering*, pp. 23–38. https://doi.org/10.1080/01457630600559538.

[4] Khan, N., and Riccio, A., 2024, "A Systematic Review of Design for Additive Manufacturing of Aerospace Lattice Structures: Current Trends and Future Directions," Progress in Aerospace Sciences, **149**. https://doi.org/10.1016/j.paerosci.2024.101021.

[5] Khan, S. A., Rahman, M. A., Khraisheh, M., and Hassan, I. G., 2024, "Advances in 3D Printed Periodic Lattice Structures for Energy Research: Energy Storage, Transport and Conversion Applications," Materials & Design, **239**. https://doi.org/10.1016/j.matdes.2024.112773.

[6] Wadley, H. N. G., 2006, "Multifunctional Periodic Cellular Metals," Philosophical Transactions of the Royal Society A: Mathematical, Physical and Engineering Sciences, **364**(1838). https://doi.org/10.1098/rsta.2005.1697.

[7] Kim, T., Zhao, C. Y., Lu, T. J., and Hodson, H. P., 2004, "Convective Heat Dissipation with Lattice-Frame Materials," *Mechanics of Materials*. https://doi.org/10.1016/j.mechmat.2003.07.001.

[8] Hyun, S., Karlsson, A. M., Torquato, S., and Evans, A. G., 2003, "Simulated Properties of Kagomé and Tetragonal Truss Core Panels," International Journal of Solids and Structures, **40**(25), pp. 6989–6998. https://doi.org/10.1016/S0020-7683(03)00350-0.

[9] Yan, H. B., Zhang, Q. C., Lu, T. J., and Kim, T., 2015, "A Lightweight X-Type Metallic Lattice in Single-Phase Forced Convection," International Journal of Heat and Mass Transfer, **83**. https://doi.org/10.1016/j.ijheatmasstransfer.2014.11.061.

[10] Joo, J. H., Kang, K. J., Kim, T., and Lu, T. J., 2011, "Forced Convective Heat Transfer in All Metallic Wire-Woven Bulk Kagome Sandwich Panels," International Journal of Heat and Mass Transfer, **54**(25–26). https://doi.org/10.1016/j.ijheatmasstransfer.2011.08.018.

[11] Shen, B., Yan, H., Xue, H., and Xie, G., 2018, "The Effects of Geometrical Topology on Fluid Flow and Thermal Performance in Kagome Cored Sandwich Panels," Applied Thermal Engineering, **142**. https://doi.org/10.1016/j.applthermaleng.2018.06.080.

[12] Corasaniti, S., Potenza, M., and Petracci, I., 2023, "Preliminary Results of Heat Transfer and Pressure Drop Measurements on Al2O3/H2O Nanofluids through a Lattice Channel," Energies (Basel), **16**(9). https://doi.org/10.3390/en16093835.

[13] Petracci, I., Corasaniti, S., Potenza, M., Tosatti, G., Santoro, D., and Consolini, L., 2025, "Thermo-Fluid Dynamic Behaviour of a Small Length 3D Printed Lattice Channel in a Conjugated Problem," International Journal of Heat and Mass Transfer, **240**. https://doi.org/10.1016/j.ijheatmasstransfer.2024.126644.

[14] Tosatti, G., Corasaniti, S., Potenza, M., and Petracci, I., 2025, Preliminary CFD Analysis on the Effects of Conjugate Problems for a Smooth Duct and a Kagome Lattice Channel: Average Results for Heat Transfer and Pressure Losses. Proceedings of the World Congress on Mechanical, Chemical, and Material Engineering, Aug. 2025, doi: https://doi.org/10.11159/htff25.179.

[15] Menter, F. R., 1994, “Two-Equation Eddy-Viscosity Turbulence Models for Engineering Applications,” AIAA Journal, **32**(8). https://doi.org/10.2514/3.12149.
[16] Wilcox, D. C., 1988, “Reassessment of the Scale-Determining Equation for Advanced Turbulence Models,” AIAA Journal, **26**(11). https://doi.org/10.2514/3.10041.